Spall fracture in wrought and additively manufactured Ni-based superalloys subjected to high pressure laser-driven shocks

Etienne Barraud, Thibaut de Rességuier, Samuel Hémery, Jonathan Cormier, Tommaso Vinci, Alessandra Benuzzi-Mounaix, Yoann Raffray, Didier Loison

This is an "author version" of a manuscript published in Materials Science and Engineering A, **911**, 146944, 2024, https://doi.org/10.1016/j.msea.2024.146944

Spall fracture in wrought and additively manufactured Ni-based superalloys subjected to high pressure laser-driven shocks

Etienne Barraud[1], Thibaut de Rességuier[1, a)], Samuel Hémery[1], Jonathan Cormier[1], Tommaso Vinci[2], Alessandra Benuzzi-Mounaix[2], Yoann Raffray[3], Didier Loison[3]

[1] Institut Pprime, CNRS, ISAE-ENSMA, Univ. Poitiers, 1 ave. Clément Ader, 86961 Futuroscope, France

[2] LULI, CNRS, CEA, Sorbonne Université, Ecole Polytechnique, Institut Polytechnique de Paris, 91128 Palaiseau, France

[3] IPR, Univ. Rennes, CNRS, 35000 Rennes, France

[a)] Corresponding author: resseguier@ensma.fr

Keywords: *Nickel-based superalloy, Rene 65, additive manufacturing, laser-driven shock, spall fracture*

Abstract

The impact response of Nickel-based superalloys is still poorly documented with respect to the industrial interest in these materials. Here, laser-driven shocks are used to study and compare the dynamic behavior of Rene 65 superalloy with different microstructures at very high strain rates in the order of 10^6 s^{-1}. Rene 65 specimens studied here are either in cast and wrought or additively manufactured (laser powder bed fusion) and subjected to different heat treatment conditions. Time-resolved velocity measurements provide the yield strength (Hugoniot elastic limit) and spall strength (resistance to dynamic tension) of each variant. In addition, post-recovery characterization gives insight into the initiation and propagation of dynamic fracture, which are shown to depend on the different manufacturing routes and thermal histories.

1. Introduction

Nickel-based superalloys are used in many of the driving sectors of industry due to their remarkable combination of mechanical properties and corrosion resistance at high temperatures. In particular, they are key materials for the extraction of fossil resources, power generation and aerospace applications such as aero-engines. The literature on the mechanical behavior of these alloys subjected to quasi-static loadings [1–4], or cyclic loadings [5–7], is abundant, but much less yet on their behavior under dynamic loading [8,9], in particular at very high strain rates [10–13]. The response of these high performance materials to intense shocks thus remains a largely unexplored issue although they may face severe pulsed loads

[14], e.g. within aircraft engines in case of in-service failure or in-flight collision, bird strike or particle ingestion.

Conventional processing routes, including steps such as casting, forging and machining, have long been the only means of manufacturing these alloys for structural parts. In recent years, a new family of processes has emerged in the industry: Additive Manufacturing (AM). Its rapid development extends to "high performance" sectors such as the aerospace industry, which seeks to remain competitive in a sustainable environment. These processes offer opportunities on two main fronts: technological, with the realisation of complex shapes and simplified assemblies, and economic, with fewer tools and less matter than in conventional ways. While many reports summarize the challenges of AM [15–17], some of which specific to superalloys [18–21], studies focussing on the consequences of AM on the high strain rate behavior of materials are still scarce [22–28], although this question attracts increasing interest [29,30].

In this paper, we study the response to laser driven shocks of the Rene 65 Ni-based superalloy, [4,6,31,32], which is widely used in the latest generation of aircraft engines. The results complement data obtained at lower strain rates and lower shock pressures in previous impact experiments reported recently [13]. Samples manufactured by laser powder bed fusion (LPBF) and cast and wrought (C&W) were considered as they display different microstructures. To evaluate the anisotropic character of deformation and fracture, the AM targets were shocked in two directions, either parallel or normal to the building direction. Planar shock loading is driven by direct irradiation of a high intensity laser pulse. Time-resolved velocity measurements provide the Hugoniot Elastic Limit and spall strength of the different variants tested. Using complementary characterization techniques, post-recovery analyses give insight into the initiation and propagation of spall damage and their dependence on the initial microstructures.

2. Materials

The nominal composition of the Rene 65 alloy employed in the present study is reported in Table I. AM-Rene 65 was produced by Laser Powder Bed Fusion. This technique involves local melting of a powder bed for layer-by-layer manufacturing. The building direction will be referred to as Z throughout the present manuscript. A hot isostatic pressing was then performed to reduce porosity. A cast and wrought reference Rene 65 was tested too for comparison between AM and conventional processes. C&W specimens were machined out from forgings submitted to a 1h/1070°C/Air quench solution heat treatment + 8h/760°C/Air quench aging. After building, AM specimens were subjected to a solution heat treatment at 1065 ° C (subsolvus specimens) or 1150 °C (supersolvus specimens) for 1 h and cooled to room temperature at 2°C/min. They were then aged for 8h at 760 °C followed by air quench. More details on these processes can be found elsewhere [33].

Table I. Nominal composition (in wt. pct) of the Rene 65 alloy.

	Ni	Cr	Mo	W	Co	Fe	Nb	Ti	Al	Zr	B
Rene 65	Base	16	4	4	13	1	0.7	3.7	2.1	0.05	0.02

Rods with a diameter about 14 mm were extracted along the Z direction and perpendicularly to this direction from the bulk AM part. They were then sectioned into thin plates by electrical discharge machining. Plate thickness was reduced to about 400 µm by mechanical polishing with 500 grit silicon carbide paper. The final samples consist of thin disks with a mean thickness of 404 µm and a standard deviation of 19 µm (about 5 %).

The microstructural features of these different variants of Rene 65 have been characterized using scanning electron microscopy (SEM) and electron backscatter diffraction (EBSD) [6,13,31,33,34]. A specific polishing procedure was applied using suspensions of diamond particles of decreasing size before a final step involving a colloidal silica solution containing 0.04 µm particles. Fig. 1 illustrates the different microstructures of the three types of target materials. The C&W Rene 65 (Fig. 1a) presents a refined microstructure composed of equiaxed grains with an average diameter about 10 µm. Also, a high twin density is observed. These features are consistent with literature data [6,13]. Primary γ' precipitates with an average diameter from 1 to 5 µm are located at grain boundaries, where non-metallic inclusions are present too. In contrast, the subsolvus-treated AM Rene 65 exhibits a strongly anisotropic microstructure (Fig. 1b,c) as also reported by Wessman et al. [6]. No inclusions, twins, nor primary γ' precipitates are detected. Grains are elongated along the building direction Z. They are about 100 µm in length. The inverse pole figure map displayed in Fig. 1b reveals a preferred orientation of the FCC crystals. The [001] direction of the FCC lattice is closely aligned with the Z direction in most grains. These columnar grains compose the successive layers of the AM process, separated by thin regions of small grains (black dotted lines) resulting from recrystallization after strong laser heating. In the plane normal to the build direction (Fig. 1c), the melting tracks can also be recognized. The microstructure of the supersolvus-treated AM Rene 65 is shown in Fig. 1d. It is composed of equiaxed grains with an average grain size of about 100 µm and no preferred crystallographic orientation such as found in the subsolvus treated material. A high twin density is observed, like in C&W Rene 65 and in previous studies [6].

The density ρ_0 and elastic sound velocities, longitudinal C_l and transverse C_t, were measured in both C&W and AM Rene 65 [13]. They were found to be roughly independent of the manufacturing route or the orientation of the AM samples, and consistent with data from the literature. Values are recalled in Table II.

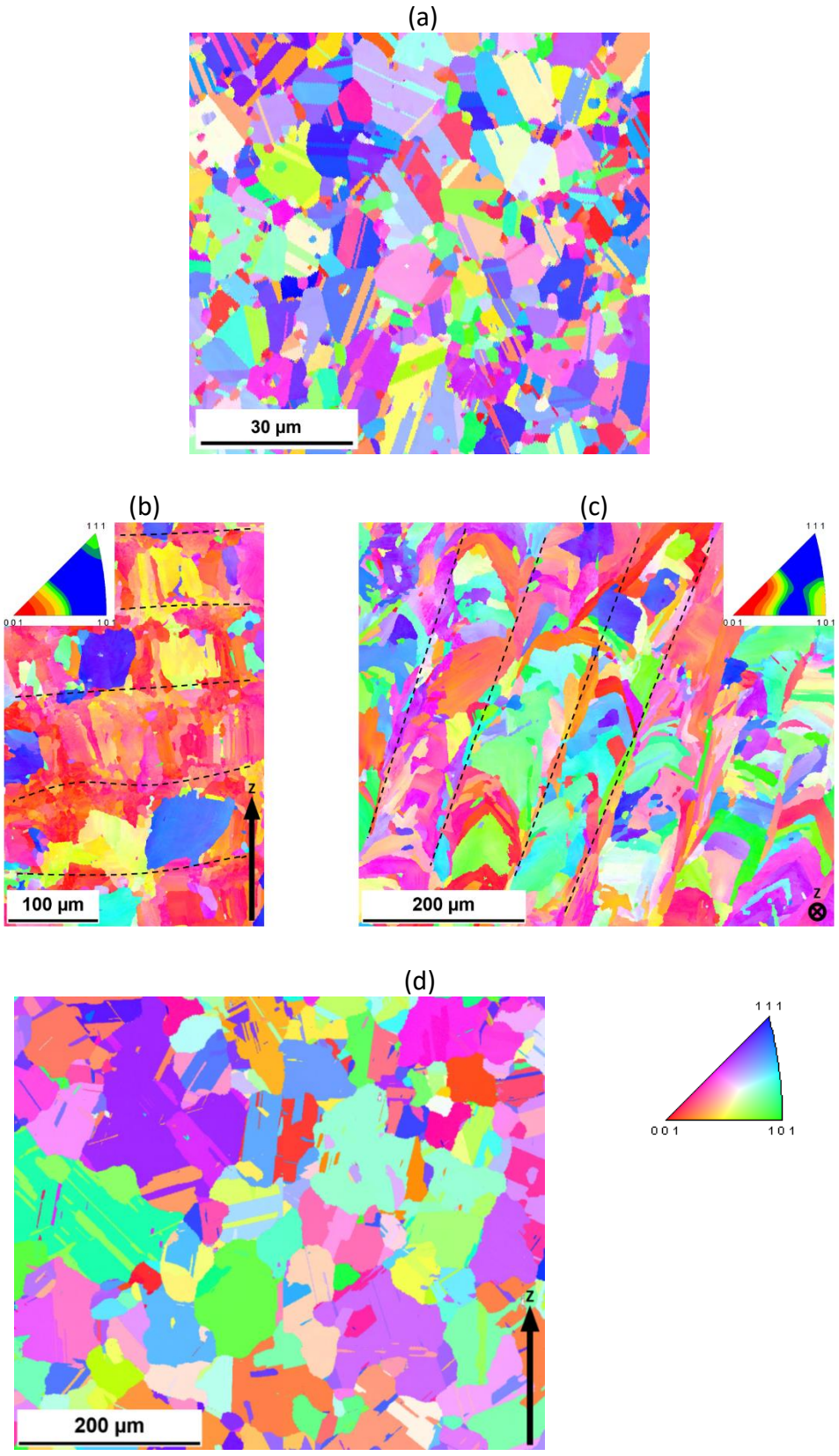

Fig. 1. Inverse pole figure maps showing crystallographic orientations in Rene 65 alloys: cast and wrought (a) (from Ref. [13]) , additively manufactured and subsolvus (b, c) or supersolvus (d) heat treated. Z is the build direction, orientations are given relative to this direction for (b, c, and d) and relative to the direction normal to the observation plane for (a).

Table II. Measured values of the density (ρ_0) and sound velocities, longitudinal (C_l) and transverse (C_t), which classically give the bulk sound velocity (C_b), for the three Rene 65 superalloys under study (from Ref. [13]).

ρ_0 (g/cm^3)	C_l (km/s)	C_t (km/s)	C_b (km/s)
8.27	5.90	3.19	4.61

3. Experimental setup

Laser shock experiments were performed at the LULI2000 facility of the *Laboratoire pour l'Utilisation des Lasers Intenses* (LULI, Ecole Polytechnique, France). A high power pulsed laser is focused on a spot of a few mm-diameter in the sample surface. A thin (µm-order) absorbing layer of the sample is ablated into a plasma cloud. Its expansion towards the laser source drives by reaction a short compressive pulse which propagates from the irradiated spot into the metal. In order to avoid laser breakdown in air and prevent oxidation after shock-induced heating, all specimens were shot in primary vacuum. Two beams (North and South) of a high power Nd-glass laser of 1053 nm-wavelength were shot alternately (Fig. 2), focused on a 2-3 mm-diameter spot in the sample surface (one single shot per sample). The maximum laser energy was about 800 J per beam, pulse duration was 5 ns or 10 ns, leading to laser intensities ranging from about 1 to 3 TW/cm².

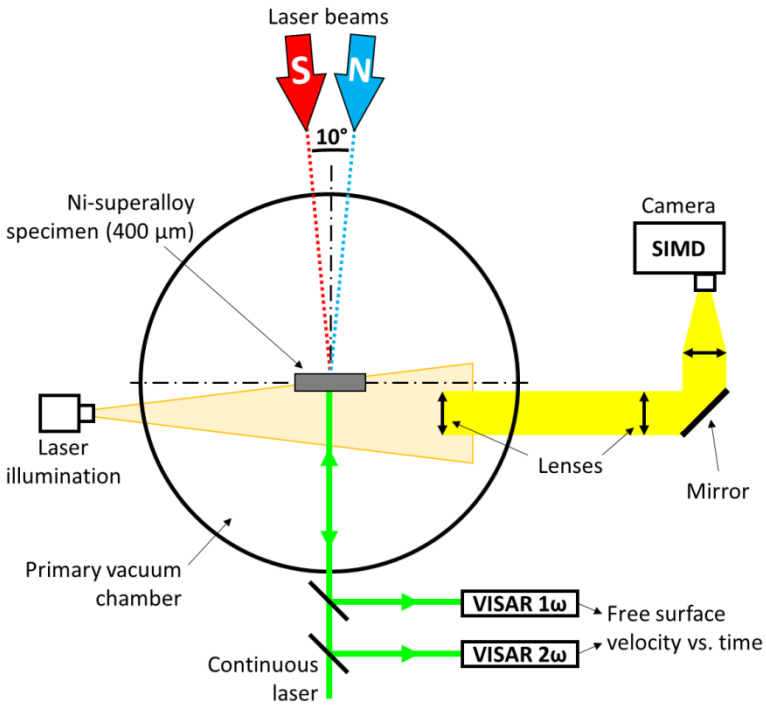

Fig. 2. Schematic view of the experimental setup.

Ultra-fast transverse shadowgraphy was implemented to visualize fragmentation and debris ejection [35,36]. Transverse illumination is provided by a continuous laser of 527 nm-wavelength. Shadowgraphs are recorded with an ultra-fast intensified camera providing 1360×1024 pixel images every 200 ns, with an ultra-short exposure time of 5 ns to ensure minimum motion blur (typically 5 µm for a fragment ejected at a 1 km/s-order velocity).
The velocity of the sample free surface, opposite to the loaded spot, is recorded by two Velocity Interferometer Systems for Any Reflector (VISAR) [37–39] developed and manufactured by the LULI team, with a time resolution of about 200 ps and a spatial resolution along a 0.5 mm line. This line is illuminated by a Nd:YAG laser, using two wavelengths, the fundamental mode at λ_0 = 1064 nm for the so-called 1ω and the second harmonic (532 nm) for the 2ω. The 1ω and 2ω beams are reflected by the free surface and sent to two VISAR interferometers having two different glass etalons leading to two different velocity-per-fringe factors, 0.498 km/s and 3.44 km/s for 2ω and 1ω, respectively. The first record gives a precise evolution of the velocity in time while the second one removes the uncertainty due to possible fringe jumps upon shock breakout. Fringe patterns are recorded with two streak cameras triggered by the laser shot (drive beam) after a controlled delay time adjusted to capture shock breakout at the free surface and subsequent velocity variations (see analysis in Section 4A) during the ~100 ns duration of the laser probe. Fig. 3 illustrates raw records at 2ω (a) and 1ω (b) for a 2.2 TW/cm² shot on a C&W sample. The colour scale is light intensity, which varies both in time and along the line in the free surface due to changes in reflectivity. Note that times 0 on the vertical axes, which differ between both cameras, are only the beginning of fringe acquisition. The real time origin in the velocity profiles coincides with the laser shot on the loaded surface; it is accurately determined from pre-shot calibration accounting for the delay mentioned above. The breakout of the pressure waves accelerates the reflecting surface, which induces a Doppler shift of the fringes. Simultaneous shifting along the 500 µm-long probed line assesses the very good planarity of the shock front emerging at the free surface. The 2ω record (Fig. 3a) shows large displacements of the fringes, which provides an accurate measurement of velocity, but the shift at shock breakout is greater than one fringe. The number of lost fringes is given by the 1ω measurement (Fig. 3b), where the high velocity-per-fringe leads to small displacements and low accuracy, but removes the indeterminacy of possible fringe jumps. To explore possible influence of heterogeneous or anisotropic microstructures on the free surface velocity, fringe shifts were analysed at three different locations along the probed line (left, center, right, see the red rectangles in Fig. 3a). However, no such influence could be evidenced, so the velocity profiles inferred from the records were averaged across those three locations for each shot.

Such free surface velocity profiles (corresponding to the raw records in Fig. 3) are shown in Fig. 4. As mentioned above, the acceleration to about 0.96 km/s at shock breakout is greater than the 0.498 km/s fringe factor in the 2ω measurement but the lost fringe is identified based on the 1ω record. The trigger delay is accounted for in such plots, i.e. time t=0 matches the laser shot on the loaded surface.

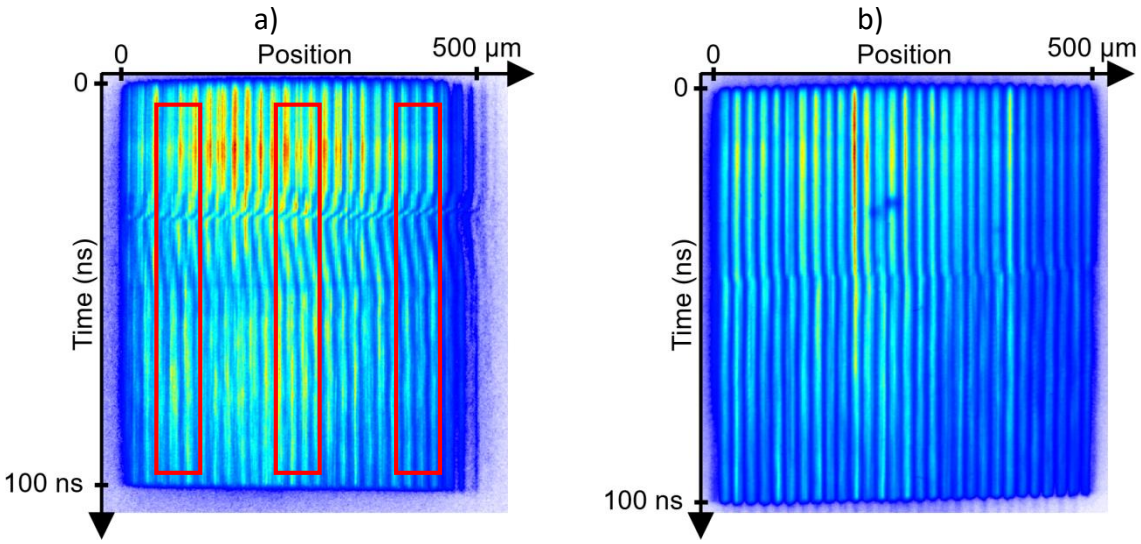

Fig. 3. Time-space profiles of interference fringes recorded simultaneously with VISAR 2ω (velocity-per-fringe=0.498 km/s) (a) and VISAR 1ω (velocity-per-fringe=3.44 km/s) (b) along a 500 µm-long line in the free surface of a 400-µm-thick superalloy sample subjected to a 2.2 TW/cm² laser shock. Rectangles show the windows where velocity profiles were extracted.

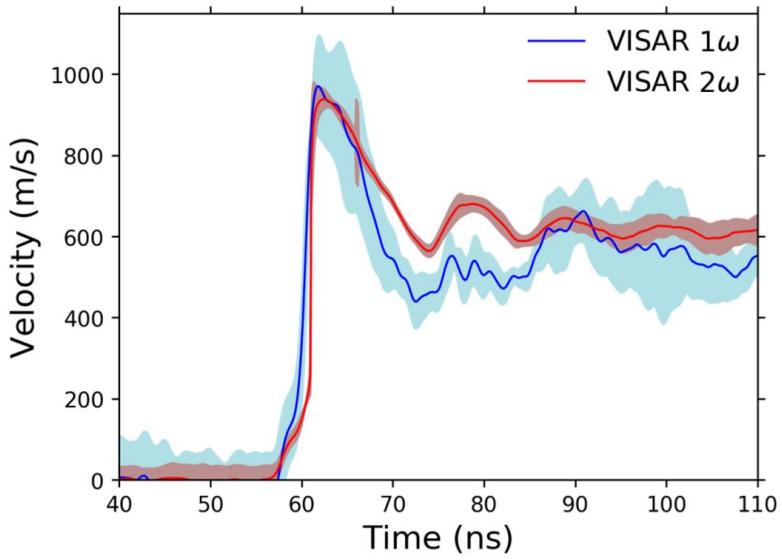

Fig. 4. Free surface velocity profiles obtained from the fringe patterns presented in Fig. 3, for a 400-µm-thick superalloy sample subjected to a 2.2 TW/cm² laser shock. Because no significant difference was observed between the three analysis windows, data were averaged across those windows, i.e. along the probed line. Shaded zones are error bars, resulting from both averaging and intrinsic resolution (better for VISAR 2ω due to lower velocity-per-fringe than for VISAR 1ω).

4. Experimental results

A. Analysis of the free surface velocity

Fig. 5 shows two typical free surface velocity profiles from VISAR measurements in two shots on AM Rene 65. Laser energy was about 800 J in both cases, laser spot diameter was between 2.5 and 3 mm, and pulse duration was either 10 ns Fig. 5a, 1.8 TW/cm² intensity) or 5 ns (Fig. 5b, 2.7 TW/cm² intensity).

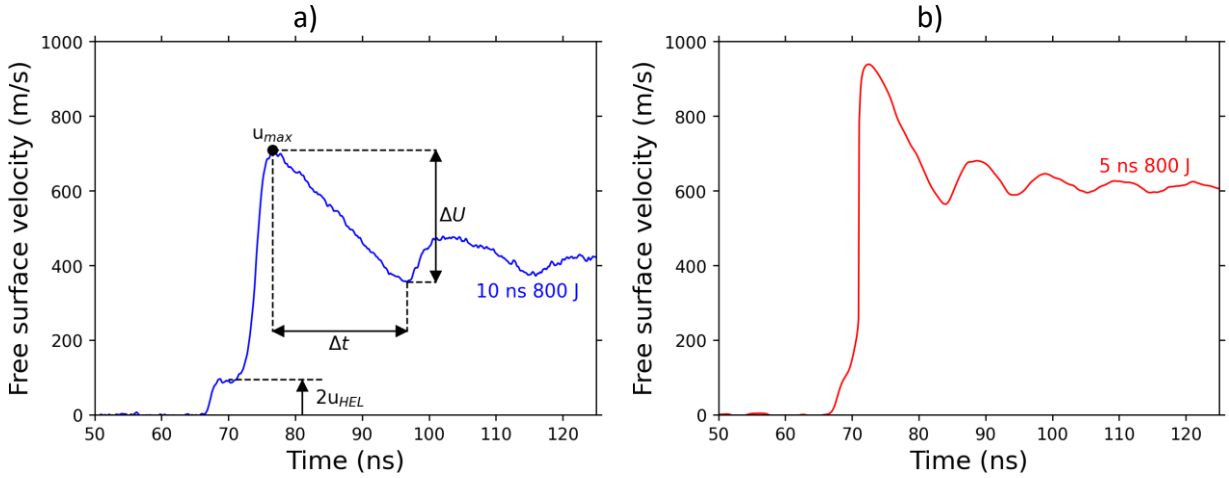

Fig. 5. Typical records of the free surface velocity in samples of Rene 65 subsolvus Z subjected to laser driven shocks of about 800 J energy and pulse duration 10 ns (a) or 5 ns (b).

Both records start with the arrival of the elastic compression wave (usually called the elastic precursor, e.g. [12,13,23,26,28,30]) at the free surface. Its amplitude called the Hugoniot Elastic Limit (HEL) is the dynamic yield strength σ_{HEL} of the material, given by

$$\sigma_{HEL} = \rho_0 \, C_l \, u_{HEL} \qquad (1)$$

where u_{HEL} is half the jump in free surface velocity (Fig. 5a). A plastic compression wave follows this elastic precursor and accelerates the free surface to its peak velocity u_{max}, which provides a rough estimate of shock pressure P_S just before breakout

$$P_S = \rho_0 \, C_b \, u_P \qquad (2)$$

where $u_P = u_{max}/2$ is the particle velocity behind the shock just before it reaches the free surface and C_b is the bulk sound speed, assumed to be close to the shock velocity in the so-called acoustic approximation. In the experiments reported here, P_s varies between 12 and 18 GPa. It increases with the loading pressure on the opposite surface, i.e. with laser intensity (see Fig. 5), but it is considerably less than this loading pressure due to pulse decay during propagation throughout the 400 µm-thick specimen. Next, the emergence of the unloading wave following the shock front produces a gradual deceleration of the free surface. Within the sample, the interaction of this incident unloading wave with the rarefaction wave produced upon reflection of the shock front from the free surface creates tensile stresses, which produce damage if they exceed the dynamic tensile strength (or spall strength) of the material [40,41]. Spall damage starts with the nucleation and growth of voids or cracks near

the plane of maximum tension. This creates new free surfaces, from which recompression waves are emitted that relax the tensile stress. The arrival of such waves reaccelerates the free surface (at about 98 ns in Fig. 5a). Finally, the record presents velocity oscillations associated with wave reverberation across the spalled layer, i.e. between the internal spall plane and the probed free surface. The amplitude ΔU of the deceleration prior to these oscillations (see Fig. 5a) is called the velocity pullback. Classic analyses of wave dynamics in an elastic-plastic material provide a value of the spall strength [40,41] which can be evaluated as

$$\sigma_{sp} = \rho_0 \, C_b \, \Delta U \, \frac{1}{1+\frac{C_b}{C_l}} \tag{3}$$

An estimate of the strain rate during tensile loading is given by

$$\dot{\varepsilon} = \frac{\Delta U}{\Delta t} \frac{1}{2C_b} \tag{4}$$

where Δt is the duration of the free surface deceleration in the record (Fig. 5a). In the present experiments, $\dot{\varepsilon}$ ranges between 1.5×10^6 s^{-1} and 4.0×10^6 s^{-1}, higher for shorter laser pulse duration (see the steeper slope in Fig. 5b than in Fig. 5a).

As pointed out in the previous section, velocity data were averaged across three positions along the probed line so the material parameters inferred at each shot are average values too.

B. Hugoniot elastic limit

The HEL values are summarized in Fig. 6. Error bars, corresponding to the standard deviation around the mean value, reflect the large scatter between the shots. We attribute this scatter to the differences in microstructures between specimens of one same type, with respect to the small lengthscales considered in the experiments (sample thickness, width of the compressed layer, length of the probed region), and to the tenuous separation between the elastic precursor and the plastic wave over such short propagation distance (especially at high shock pressures, where this separation becomes hardly detectable). Within this scatter, it is difficult to establish clear influences of the manufacturing route, the orientation or the heat treatment conditions. Nevertheless, the highest yield strength (elastic limit) in the C&W alloy and the lowest one in the supersolvus-treated AM material are qualitatively consistent with the Hall-Petch relationship [42]. Indeed, for grain sizes in the range studied here, the yield strength of polycrystals is observed to increase as the grain size decreases (e.g. [43–45]). Overall, the HEL values measured here at 1-4×10^6 s^{-1} are found to be about 2-3 GPa. For comparison, under quasi-static loading, yield strengths around 0.9 GPa have been reported for various Ni-based superalloys, including Rene 65 [4], Inconel 738LC [46], Inconel 792 [47], Udimet [48] and others [49–51]). Considering dynamic loading conditions with lower strain rates, typically 10^5 s^{-1}, Hugoniot elastic limits vary between 1 and 2.5 GPa in single-crystal PWA1483 [12] and polycrystalline Inconel 690 [11], Inconel 738 LC [12], Inconel 718 [25,27].

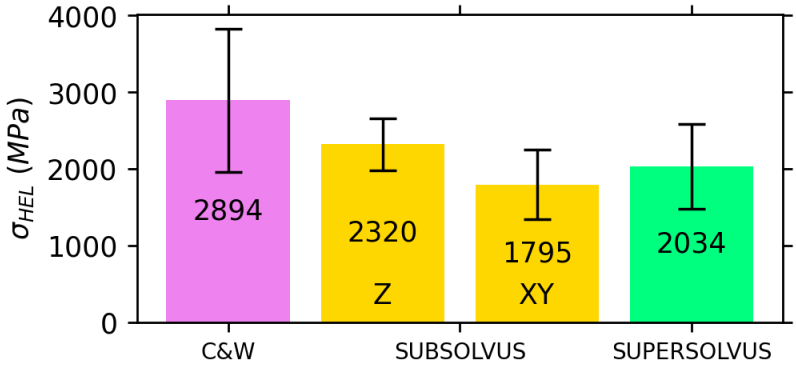

Fig. 6. Measured values of the Hugoniot Elastic Limit in four types of tested specimens. Numbers are mean values, within a standard deviation shown as error bars.

C. Spall strength

Fig. 7 shows the spall strength values inferred from the velocity records under laser-driven shock loading.

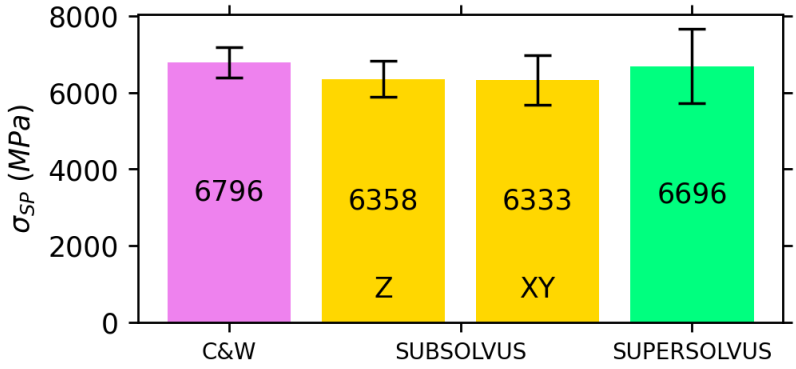

Fig. 7. Measured values of the spall strength in four types of tested specimens. Numbers are mean values, within a standard deviation shown as error bars.

The average spall strength of the Rene 65 superalloy in such dynamic loading conditions is around 6.5 GPa. Such value is comparatively high, similar to that of high-strength metals typically used in military applications such as tantalum [52]. Again, considering the significant scatter, it appears roughly insensitive to the manufacturing route, the loading direction and the heat treatment conditions. For comparison, an ultimate tensile stress around 1.3-1.6 GPa was measured for a variety of Ni-based superalloys [53] including Inconel 718, 718 Plus and Waspaloy tested using quasi-static loading conditions. At high strain rates around 1.5×10^6 s^{-1} under impact loading [12], the spall strength of single-crystal PWA 1483 was reported to be 3.5 GPa and that of polycrystalline Inconel 738LC was evaluated to 2.9 GPa. Finally, at intermediate rates produced by the impact of thin laser-launched flyers, the same variants of Rene 65 exhibited a spall strength of about 5 GPa [13]. Those results are compared with the present measurements in Fig. 8. σ_{SP} increases with $\dot{\varepsilon}$ up to about 1.5×10^6 s^{-1} then seems to saturate. In these experiments, increasing the strain rate goes with decreasing the duration of pressure application, which amounts to reducing the spatial width of the zone subjected to tension within the sample upon reflection of the pressure pulse from the free surface (blue

region in the schematic insets in Fig. 8). Thus, the probability for this region to contain sites prone to early damage initiation and development (e.g. inclusions, precipitates and grain boundaries, shown as black dots in the schematic insets in Fig. 8) decreases with increasing loading rates. This may result in the measured increase in spall strength. Saturation may arise upon further increase in loading rate as this probability becomes very small, at least beneath the line probed by the VISAR.

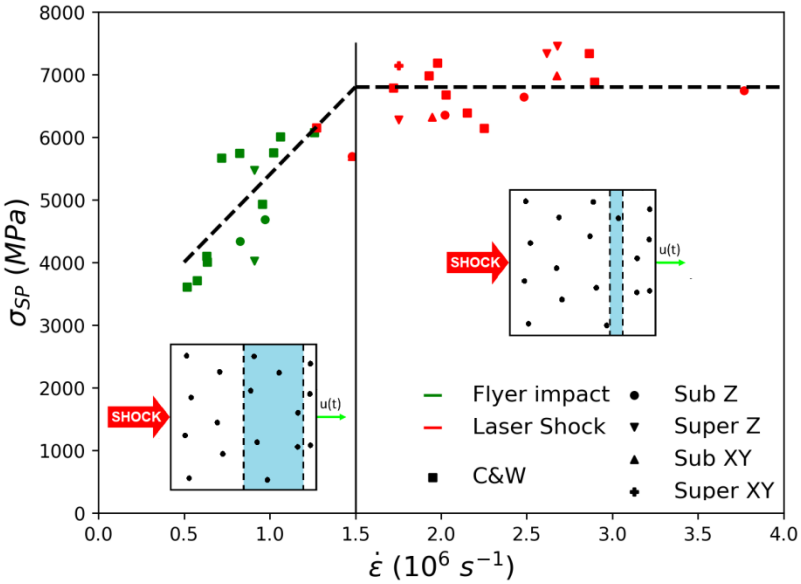

Fig. 8. Comparison of the spall strength values recorded in Rene 65 impacted by laser-launched flyers (green dots, from Ref. [13]) or subjected to direct laser shocks (red, this work). The insets show schematically how the lower width of the tensile zone might explain the higher strength at increasing strain rates.

5. Transverse shadowgraphy

Fig. 9 shows sequences of three shadowgraphs recorded at 800 ns intervals for five 400 µm-thick targets of C&W samples (a). Similar data is also reported for AM samples subsolvus treated and tested along Z (b) or XY (c), and supersolvus treated and tested along Z (d) or XY (e). The laser shot at time t_0 triggers the camera. The shock then travels at a mean velocity on the order of 4.6 km/s throughout the 400 µm thickness so that breakout at the free surface is expected at about t_0+90 ns. The target holder and the unshocked part of the target do not move over the recorded time interval. The good spatial homogeneity of the laser energy in the beam ensures a good uniformity of the applied pressure on the irradiated surface, leading to planar wave fronts, as pointed out earlier from Fig. 3. Indeed, earlier shadowgraphs just after shock breakout (not shown here) show the displacement of a planar central surface of a few mm-diameter matching that of the loaded spot. At the later times shown here, the spalled layer has deformed before detaching from the bulk upon shear failure at its periphery, so that its contour is curved. In the C&W sample (Fig. 9a) the spall is then ejected in vacuum at a constant speed of about 540 m/s without further deformation and it remains well parallel to the target surface. Under similar conditions, similar ejection has been observed in pure metals [35]. In contrast, in the AM material (Fig. 9b-e), the spalled layer is seen to break into distinct fragments before complete separation from the rest of the target, and an early loss of

symmetry around the central axis is observed, with the chaotic ejection of fragments of various sizes, sometimes with significant radial and rotational velocities. Such behavior probably results from multiple failure at different depths below the free surface, governed by damage nucleation at preferential sites as discussed in the next section.

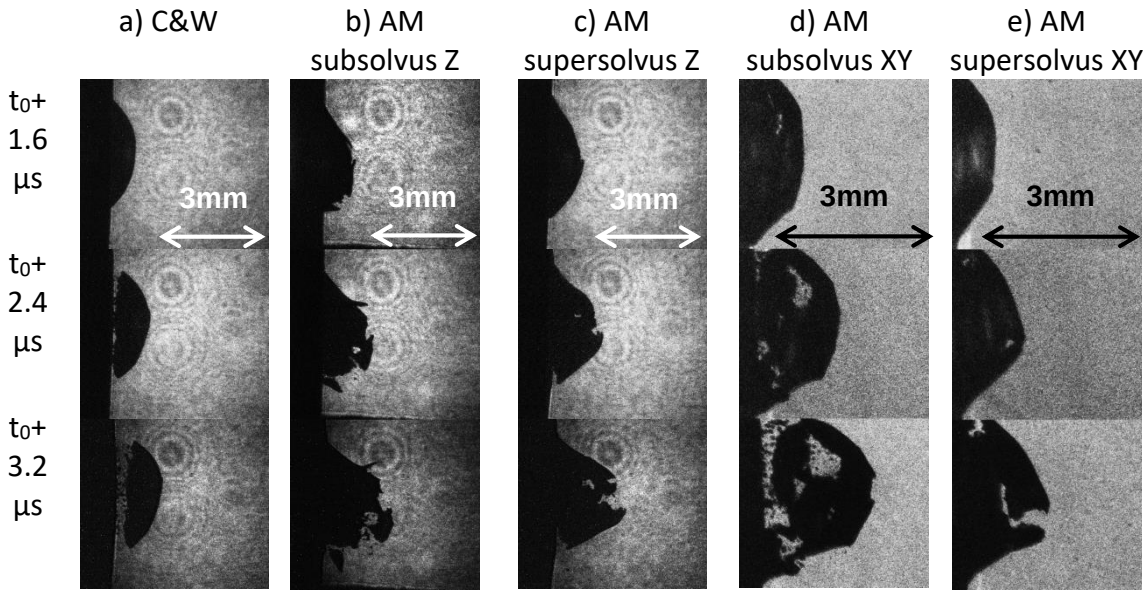

Fig. 9. Transverse shadowgraphy of spall ejection (to the right) from samples of Rene 65, cast and wrought (a) or additively manufactured (b-e), subjected to laser shock loading at time t_0.

6. Post-recovery observations

The removal of the fragments leaves a crater in the free surface of the recovered samples, where the fracture surface can be analysed. Observations were made both in the crater surface and on cross-sections.

A. C&W samples

Fig. 10 shows a typical crater surface in a C&W target subjected to a 3.5 TW/cm² laser shock. The crater is circular with sharp contours. Its 2.55 mm-diameter is close to that of the irradiated spot in the opposite loaded surface. Such observation is consistent with the ejection sequence shown in Fig. 9a. At higher magnification (Fig. 10b), the fracture surface consists of small dimples typical of ductile damage. As already illustrated and discussed in a previous article [13], voids nucleate preferentially at inclusions located at grain boundaries such as primary γ' precipitates (red arrows) and more occasional carbide particles (yellow arrow).

Cross-sectional micrographs of the spall plane in another C&W sample recovered after a 2.0 TW/cm² laser shock are shown in Fig. 11 to illustrate a case of lower damage. They confirm that primary γ' precipitates and carbide particles provide favourable sites for void nucleation (Fig. 11a). Then crack propagation follows a tortuous path mixing intergranular and transgranular fracture (Fig. 11b), which is consistent with previous observations reported under impact loading [13].

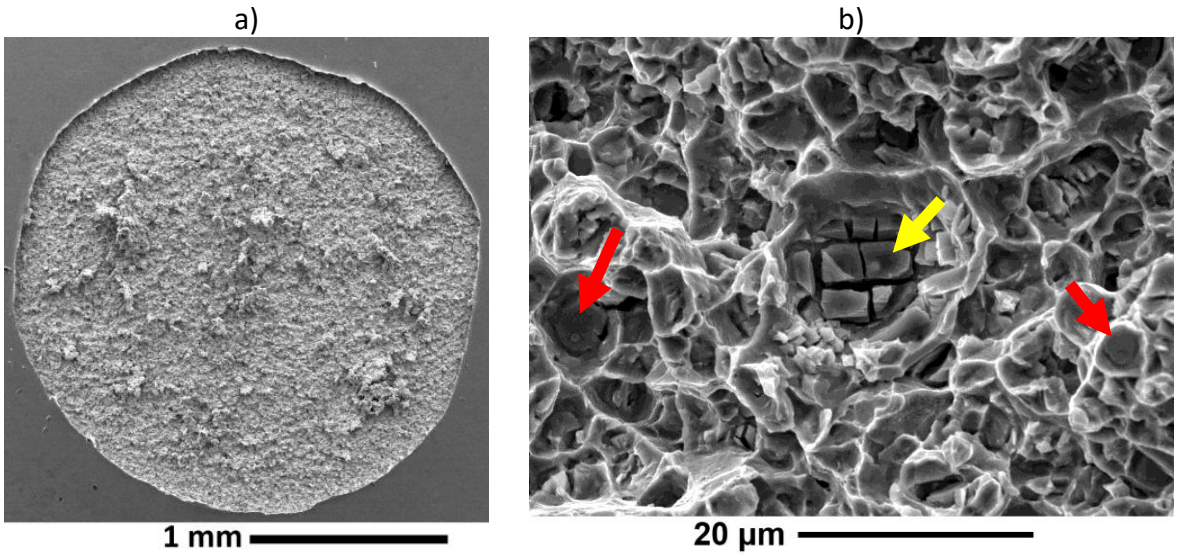

Fig. 10. SEM micrographs showing the spall crater in the free surface of a C&W Rene 65 sample recovered after a 3.5 TW/cm² laser shock: overview (a) and magnification in the crater (b) showing dimples indicative of ductile fracture with signs of crack initiation at carbides (yellow arrow) and primary γ' precipitates (red arrows).

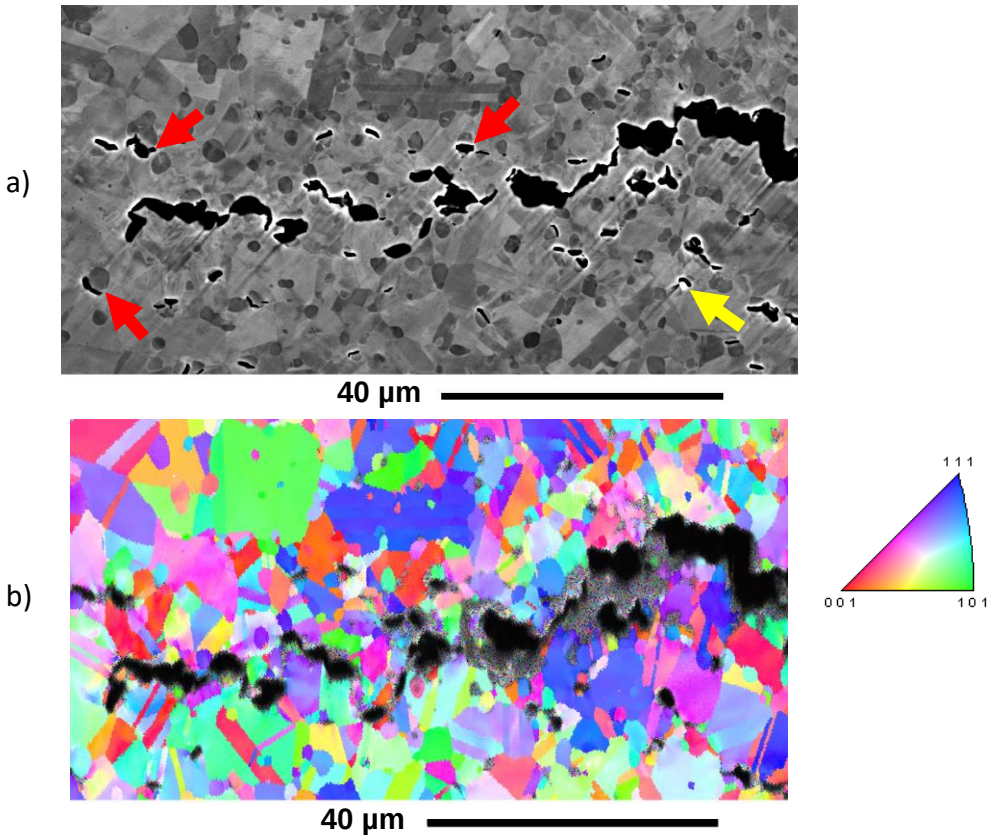

Fig. 11. SEM micrograph showing a cross sectional view of the spall plane in a C&W Rene 65 sample recovered after a 2.0 TW/cm² laser shock, applied from bottom to top (a) and inverse pole figure map superimposed with image quality showing the same region (b). Crystallographic orientations are given relative to the vertical (shock propagation) direction. Cracks nucleate preferentially at primary γ' precipitates (red arrows) and carbides (yellow arrow) then propagate from one inclusion to the next along a mixed inter/transgranular path.

B. Supersolvus-treated AM samples

In the supersolvus-treated AM targets, the crater surface shows stair-like features, with a combination of ductile transgranular fracture and deeper, smooth facets suggesting intergranular cracking (Fig. 12). No significant dependence on the direction of shock application was observed, as expected from the isotropic character of microstructural features in the supersolvus-treated specimens (Fig. 1d). Again, the observations seem consistent with the shadowgraphs showing the ejection of large, irregularly shaped fragments (Fig. 9c and Fig. 9e). Fig. 13 shows an EBSD map of a cross-section in a laser shock-loaded supersolvus-treated sample, near the edge of the loaded region, where the spalled layer (upper part) is still attached to the bulk target. It clearly shows that voids form mainly at grain boundaries, as reported under impact loading [13], and that cracks propagate throughout grains, but also along grain boundaries, deeper beneath the free surface, which supports the interpretation of Fig. 12.

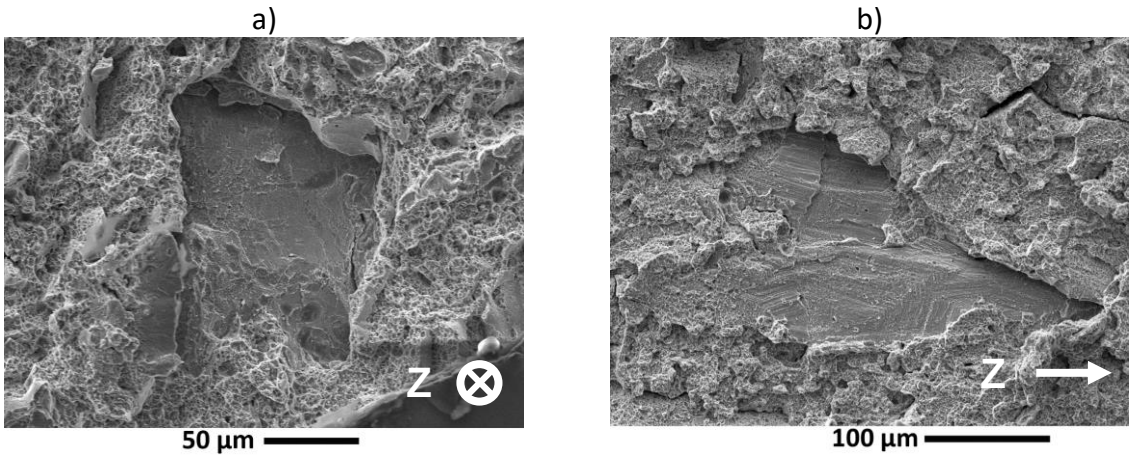

Fig. 12. SEM micrographs showing the spall crater in AM supersolvus Rene 65 samples recovered after shock loading along (a) (2.1 TW/cm²) or normal to (b) the Z direction (1.1 TW/cm²).

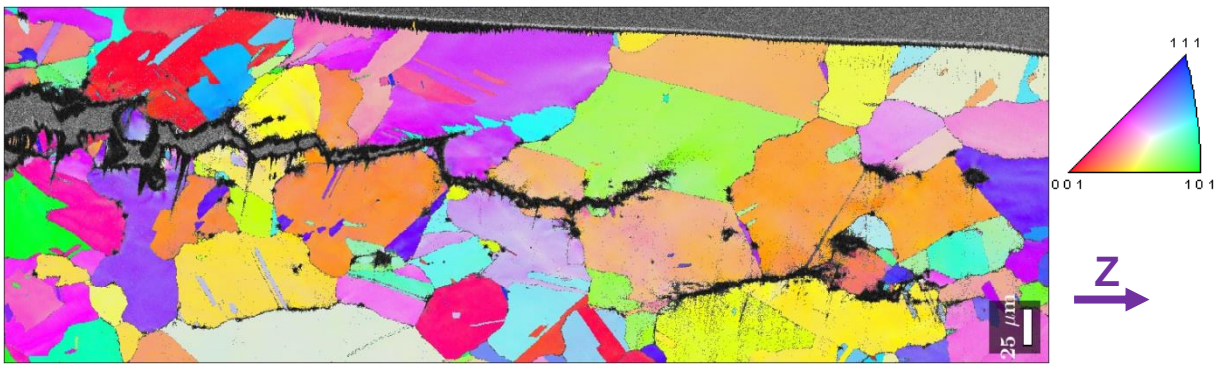

Fig. 13. Inverse pole figure map showing crystallographic orientations in the vicinity of a spall fractured region in an AM supersolvus Rene 65 sample recovered after a 1.1 TW/cm² laser shock loading applied from bottom to top, normally to the build direction Z. Superimposed image quality highlights void nucleation at grain boundaries, as well as a mixture of intergranular and transgranular cracking.

C. Subsolvus-treated AM samples

Although no significant influence of the loading direction was evidenced on the macroscopic response of the subsolvus-treated AM sample (i.e., Fig. 7), the anisotropic character of the microstructure (Fig. 1b, c) may imply differences in fracture mechanisms.

A spall crater in a specimen tested along Z (i.e., shock loading direction and the build direction are parallel) and subjected to a 1.8 TW/cm² laser shock is shown in Fig. 14. It is roughly circular with sharp edges. The closer view in Fig. 14b reveals dimples characteristic of ductile fracture as well as short, straight and sharp cracks normal to the crater surface. Fig. 15 shows micrographs of a spall crater in an XY sample (where shock loading direction and build direction were normal to each other). The crater is still roughly circular but its contours are partially hidden below large, irregular petals rising at the edges of the loaded surface. This feature suggests late separation of the spalled layer and is in good agreement with the corresponding shadowgraphs in Fig. 9d. The bottom surface is very irregular, with a stair-like aspect due to the removal of large chunks, consistent with the ejection of large fragments observed in Fig. 9d. The examination of the fracture surface reveals a mixture of dimples at the main spall plane and smooth facets in slightly deeper zones of typical size about 250 µm, suggesting intergranular/interlayer cracking (Fig. 15b). Additional cracks normal to the crater surface seem to propagate in depth perpendicular to the loading direction in that case (Fig. 15c).

Cross-sections were prepared in the subsolvus-treated AM samples where spall damage was less severe (i.e., without ejection of the spalled layers) to collect the EBSD maps shown in Fig. 16. Samples subjected to shock loading along or normal to the build direction Z were considered. The Z sample (Fig. 16a) presents mainly transgranular fracture across the columnar grains, as already evidenced and discussed elsewhere [13]. However, void nucleation is visible at some grain boundaries. In the XY sample, where loading direction was normal to the build direction (Fig. 16b, c), the cross section was prepared so that the observation plane contains the Z direction. Evidence of preferential void nucleation at grain boundaries is observed (Fig. 16b). However, in contrast with the Z sample, cracking is mostly intergranular, running between the columnar grains (Fig. 16c).

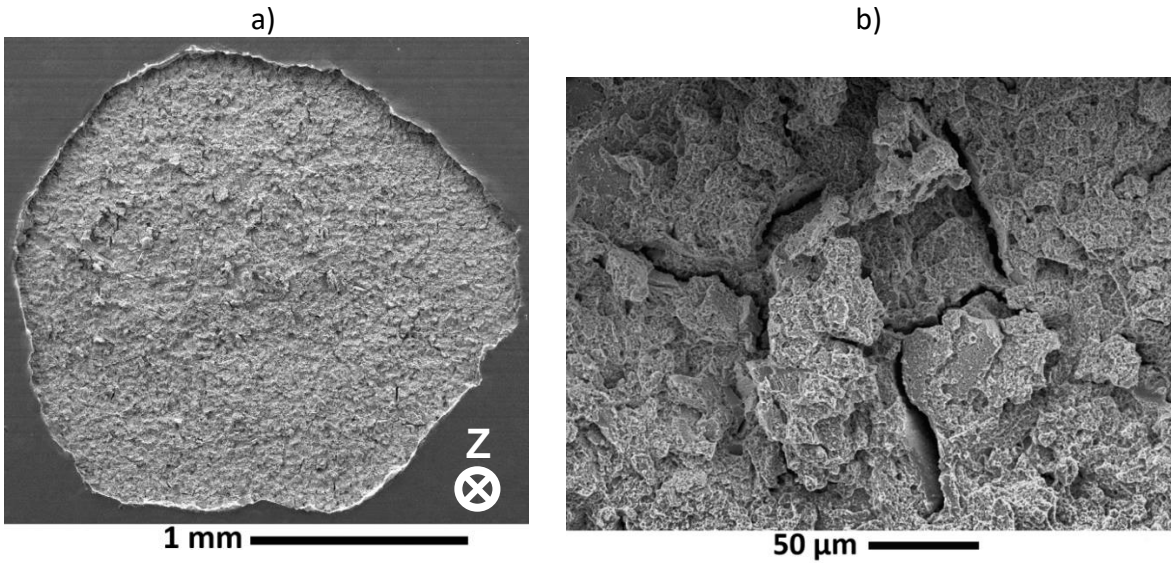

Fig. 14. SEM micrographs showing the spall crater in an AM subsolvus Rene 65 sample recovered after a 1.8 TW/cm² laser shock loading along the build direction Z.

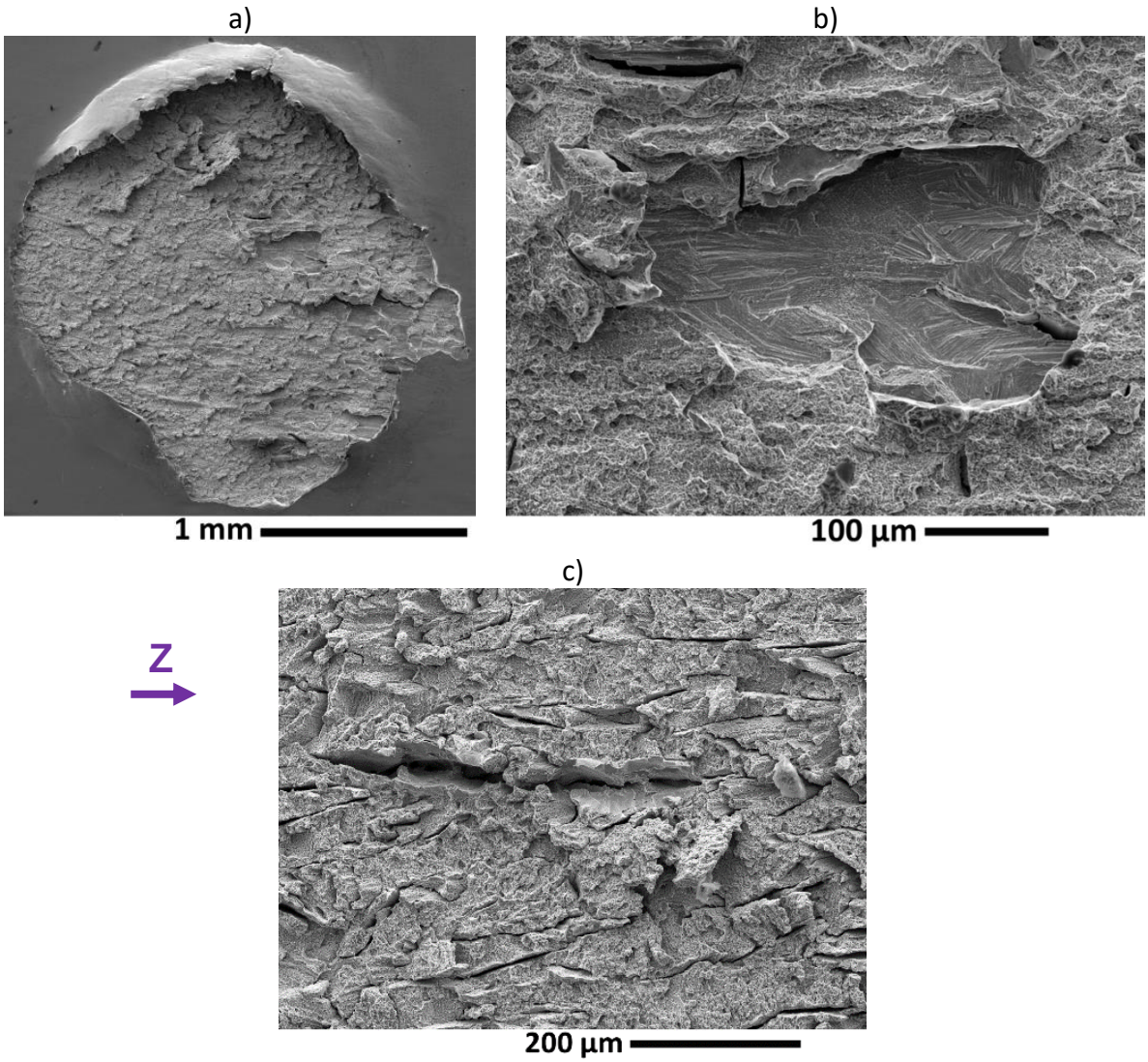

Fig. 15. SEM micrographs showing the spall crater in an AM subsolvus Rene 65 sample recovered after a laser shock normal to the build direction Z.

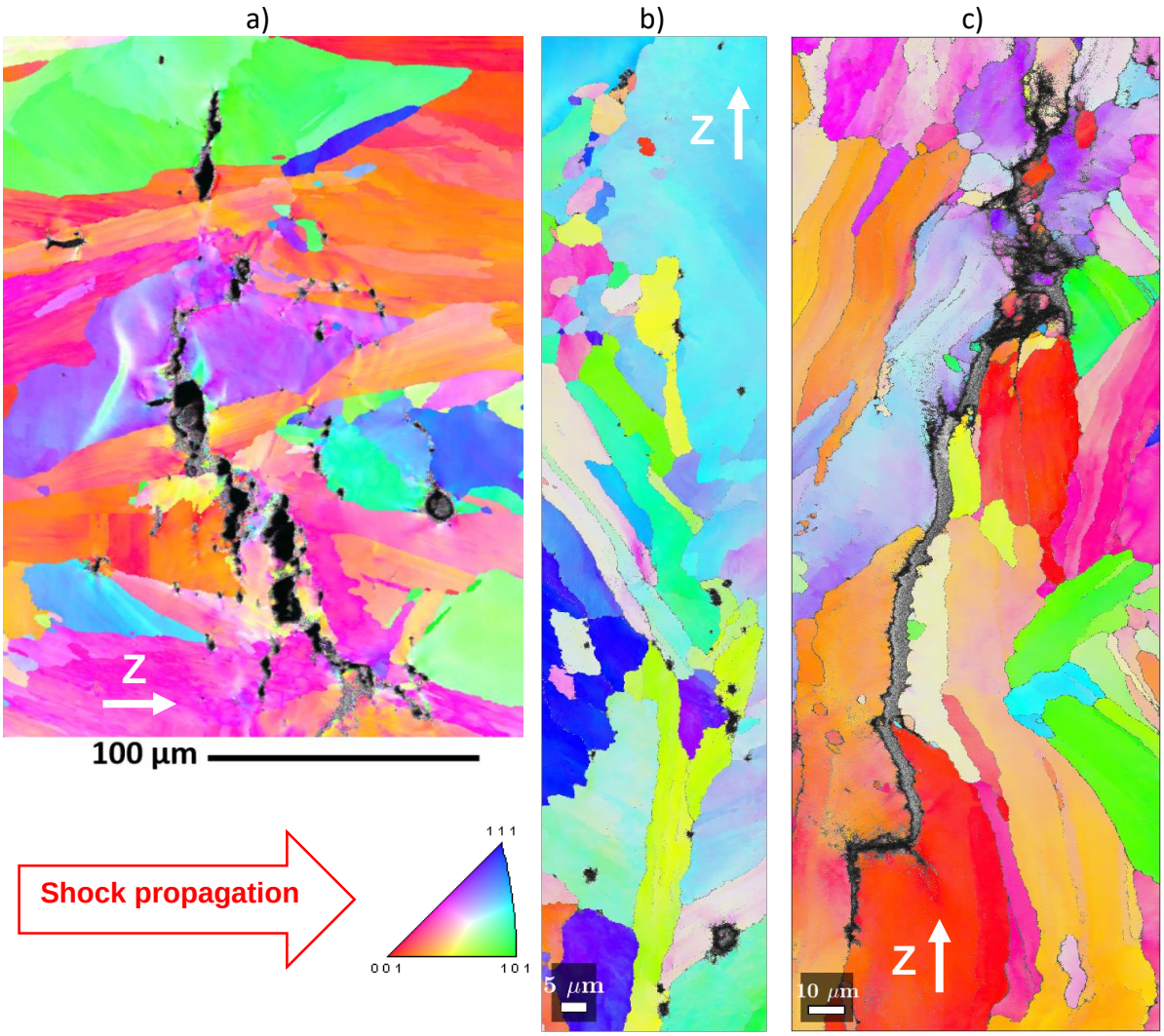

Fig. 16. Inverse pole figure maps showing crystallographic orientations of cross sections in AM subsolvus Rene 65 samples recovered after shock loading along (a) or normal to (b, c) the Z direction. Superimposed image quality highlights void nucleation at grain boundaries for all samples, as well as intergranular cracking in the XY sample versus transgranular cracking in the Z sample.

Fig. 17 schematically summarizes the direction-dependent spall processes operating in the subsolvus-treated AM Rene 65 samples inferred from the above observations. Shock loading is applied onto the left surface. Wave interactions generate tension beneath the opposite free surface (pink shaded zone). In the Z specimen (Fig. 17a), void nucleation preferentially proceeds at grain boundaries, probably as a result of deformation incompatibility between grains. Subsequent fracture (red lines) is mainly of transgranular character and develops through the columnar grains. Indeed, grain boundaries are unfavourably oriented for coalescence of voids. Nevertheless, crack growth parallel to the loading direction is occasionally observed along grain boundaries, despite being oriented unfavourably with respect to the main loading direction (see Fig. 14). Indeed, the tensile stress component acting on the grain boundaries should be low as most of them are parallel to the shock direction. This feature highlights the weak character of grain boundaries in the subsolvus treated AM

samples. In an XY specimen where the loading direction is normal to the Z axis (Fig. 17b), a more balanced contribution of transgranular and intergranular cracking is observed. While void nucleation proceeds at grain boundaries, as also observed in the Z samples, grain boundaries are mostly oriented normal to the loading direction. Hence, they can serve as preferential crack path. However, transgranular cracking is likely needed depending on the presence of grain boundaries in the close vicinity of the plane of maximum tension (see Fig. 15), and the features of these grain boundary, that determine their resistance to cracking. Besides, residual tension after a first fracture may be high enough to produce cracks at grain boundaries located deeper below the free surface. Such multiple spall scenario is consistent both with the ejection of successive spalled layers (Fig. 9d) and with the final stair-like fracture profile (Fig. 15b).

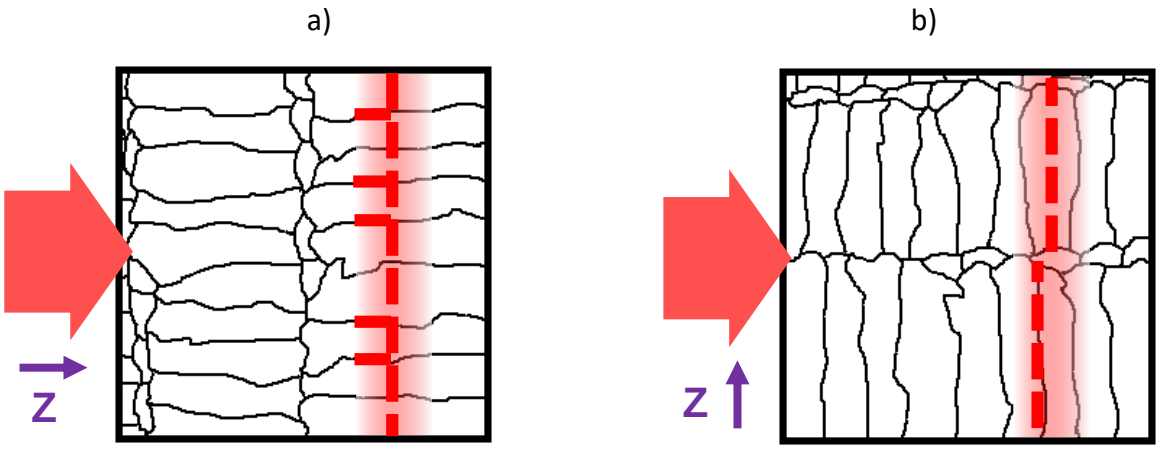

Fig. 17. Schematic representation of spall fracture in an AM subsolvus sample subjected to laser shock loading along (a) or normal to (b) the build direction Z.

7. Conclusion

High power laser irradiation of ns-order duration was used to study the shock behavior of the Ni-based superalloy Rene 65 at extremely high strain rates above 10^6 s^{-1}. Tested specimens were either cast and wrought (C&W) or additively manufactured (AM). Subsolvus and supersolvus heat treatments were applied to AM samples to investigate the influence of microstructure features on the material response. Time-resolved velocity measurements provided both the Hugoniot elastic limit (compressive yield strength) and spall strength (dynamic tensile strength), respectively about 2.3 GPa and 6.5 GPa. This is consistent with values reported previously upon high velocity impact of laser-launched flyers, under conditions of slightly lower strain rates leading to slightly lower values. Both values are comparatively very high, indicative of an excellent resistance of this superalloy to dynamic loading. Within the relatively large scatter attributed to shot to shot differences in local sample microstructures, these measurements did not show a significant influence of the manufacturing route, the heat treatment, and the loading direction relative to the build orientation of AM samples. Post-recovery characterization was carried out as laser-driven shocks are much less destructive than more conventional loading techniques. It provided clear insights into the processes governing spall damage and subsequent fragment ejection. Thus, void nucleation and crack propagation were found to depend on the sample microstructure directly inherited from the manufacturing route and the heat treatment. In particular, the

columnar character of the grains in the subsolvus treated AM sample was shown to induce an anisotropic fracture behavior at the micro-scale. Nevertheless, the macroscopic response, including the fracture strength, was relatively insensitive to the differences in mechanism, i.e. primarily governed by inertia effects rather than microstructural features at such high loading rates. Future work will include laser shock experiments on pre-heated samples to explore the effects of high initial temperature, representative of service conditions within aero-engines, on the dynamic behavior of this superalloy.

Acknowledgements

The authors are grateful to Emilien Lescoute, Benjamin Jodar, Arnaud Sollier and Jean-Marc Chevalier for their help with the transverse shadowgraphy setup, and to all the LULI technical staff for operating the LULI2000 facility. Amélie Caradec is thanked for her kind help with the SEM. GE Additive and, more specifically, Dr. Andrew Wessman (formerly at GE Additive and now at the University of Arizona in Tucson) are acknowledged for providing AM processed Rene 65 specimens.

Data availability

The raw/processed data required to reproduce these findings cannot be shared at this time as the data also forms part of an ongoing study.

References

[1] M.J. Donachie, S.J. Donachie, Superalloys: A Technical Guide, 2nd ed., ASM International, 2002. https://doi.org/10.31399/asm.tb.stg2.9781627082679.

[2] T.M. Pollock, S. Tin, Nickel-Based Superalloys for Advanced Turbine Engines: Chemistry, Microstructure and Properties, Journal of Propulsion and Power **22**, 361–374, 2006. https://doi.org/10.2514/1.18239.

[3] R.C. Reed, The Superalloys: Fundamentals and Applications, Cambridge University Press, 2006. https://doi.org/10.1017/CBO9780511541285.

[4] J.A. Heaney, M.L. Lasonde, A.M. Powell, Development of a new cast and wrought alloy (René 65) for high temperature disk applications, in: 8th International Symposium on Superalloy 718 and Derivatives, John Wiley & Sons, Inc., Hoboken, NJ, USA, pp. 67–77, 2014. https://doi.org/10.1002/9781119016854.ch6.

[5] A. Pineau, S.D. Antolovich, High temperature fatigue of nickel-base superalloys – A review with special emphasis on deformation modes and oxidation, Engineering Failure Analysis **16**, 2668–2697, 2009. https://doi.org/10.1016/j.engfailanal.2009.01.010.

[6] A. Wessman, A. Laurence, J. Cormier, P. Villechaise, T. Billot, J.M. Franchet, Thermal Stability of Cast and Wrought Alloy Rene 65, in: Proceedings of the 13th International Symposium on Superalloys, The Minerals, Metals & Materials Society, pp. 793–800, 2016. https://doi.org/10.7449/Superalloys/2016/Superalloys_2016_793_800.

[7] D. Texier, J. Cormier, P. Villechaise, J.-C. Stinville, C.J. Torbet, S. Pierret, T.M. Pollock, Crack initiation sensitivity of wrought direct aged alloy 718 in the very high cycle fatigue regime: the role of non-metallic inclusions, Materials Science and Engineering: A **678**, 122–136, 2016. https://doi.org/10.1016/j.msea.2016.09.098.

[8] B. Erice, M.J. Pérez-Martín, F. Gálvez, An experimental and numerical study of ductile failure under quasi-static and impact loadings of Inconel 718 nickel-base superalloy, International Journal of Impact Engineering **69**, 11–24, 2014. https://doi.org/10.1016/j.ijimpeng.2014.02.007.

[9] J. Wang, W.-G. Guo, Y. Su, P. Zhou, K. Yuan, Anomalous behaviors of a single-crystal Nickel-base superalloy over a wide range of temperatures and strain rates, Mechanics of Materials **94**, 79–90, 2016. https://doi.org/10.1016/j.mechmat.2015.11.015.
[10] K.S. Vecchio, G.T. Gray, Effects of shock loading on a solid-solution strengthened superalloy, in: AIP Conference Proceedings, AIP, Colorado Springs, Colorado (USA), pp. 1213–1216, 1994. https://doi.org/10.1063/1.46063.
[11] W.-S. Lee, C.-Y. Liu, T.-N. Sun, Dynamic impact response and microstructural evolution of inconel 690 superalloy at elevated temperatures, International Journal of Impact Engineering **32**, 210–223, 2005. https://doi.org/10.1016/j.ijimpeng.2004.09.007.
[12] E.B. Zaretsky, G.I. Kanel, S.V. Razorenov, K. Baumung, Impact strength properties of nickel-based refractory superalloys at normal and elevated temperatures, International Journal of Impact Engineering **31**, 41–54, 2005. https://doi.org/10.1016/j.ijimpeng.2003.11.004.
[13] E. Barraud, T. de Rességuier, J. Baillargeat, S. Hemery, J. Cormier, Dynamic response of wrought and additively manufactured Nickel-based alloys to high velocity impacts of laser-launched flyers, Journal of Applied Physics **131**, 225105, 2022. https://doi.org/10.1063/5.0085285.
[14] J.M. Pereira, B.A. Lerch, Effects of heat treatment on the ballistic impact properties of Inconel 718 for jet engine fan containment applications, International Journal of Impact Engineering **25**, 715–733, 2001. https://doi.org/10.1016/S0734-743X(01)00018-5.
[15] W.E. Frazier, Metal Additive Manufacturing: A Review, Journal of Materials Engineering and Performance **23**, 1917–1928, 2014. https://doi.org/10.1007/s11665-014-0958-z.
[16] C.Y. Yap, C.K. Chua, Z.L. Dong, Z.H. Liu, D.Q. Zhang, L.E. Loh, S.L. Sing, Review of selective laser melting: Materials and applications, Applied Physics Reviews **2**, 041101, 2015. https://doi.org/10.1063/1.4935926.
[17] J. Gunasekaran, P. Sevvel, I. John Solomon, P. Tanushkumaar, A brief review on the manufacturing of metal components using selective laser melting, Materials Today: Proceedings **64**, 173–180, 2022. https://doi.org/10.1016/j.matpr.2022.04.213.
[18] W.J. Sames, F.A. List, S. Pannala, R.R. Dehoff, S.S. Babu, The metallurgy and processing science of metal additive manufacturing, International Materials Reviews **61**, 315–360, 2016. https://doi.org/10.1080/09506608.2015.1116649.
[19] S.E. Atabay, O. Sanchez-Mata, J.A. Muñiz-Lerma, R. Gauvin, M. Brochu, Microstructure and mechanical properties of rene 41 alloy manufactured by laser powder bed fusion, Materials Science and Engineering: A **773**, 138849, 2020. https://doi.org/10.1016/j.msea.2019.138849.
[20] Y.T. Tang, C. Panwisawas, J.N. Ghoussoub, Y. Gong, J.W.G. Clark, A.A.N. Németh, D.G. McCartney, R.C. Reed, Alloys-by-design: Application to new superalloys for additive manufacturing, Acta Materialia **202**, 417–436, 2021. https://doi.org/10.1016/j.actamat.2020.09.023.
[21] M. Moradi, Z. Pourmand, A. Hasani, M. Karami Moghadam, A.H. Sakhaei, M. Shafiee, J. Lawrence, Direct laser metal deposition (DLMD) additive manufacturing (AM) of Inconel 718 superalloy: Elemental, microstructural and physical properties evaluation, Optik **259**, 169018, 2022. https://doi.org/10.1016/j.ijleo.2022.169018.
[22] D.R. Jones, S.J. Fensin, O. Dippo, R.A. Beal, V. Livescu, D.T. Martinez, C.P. Trujillo, J.N. Florando, M. Kumar, G.T. Gray, Spall fracture in additive manufactured Ti-6Al-4V, Journal of Applied Physics **120**, 135902, 2016. https://doi.org/10.1063/1.4963279.

[23] E. Zaretsky, A. Stern, N. Frage, Dynamic response of AlSi10Mg alloy fabricated by selective laser melting, Materials Science and Engineering: A **688**, 364–370, 2017. https://doi.org/10.1016/j.msea.2017.02.004.
[24] L.C. Smith, D.J. Chapman, P.A. Hooper, G. Whiteman, D.E. Eakins, On the dynamic response of additively manufactured 316L, AIP Conference Proceedings **1979**, 060007, 2018. https://doi.org/10.1063/1.5044804.
[25] G. Asala, J. Andersson, O.A. Ojo, Improved dynamic impact behaviour of wire-arc additive manufactured ATI 718Plus®, Materials Science and Engineering: A **738**, 111–124, 2018. https://doi.org/10.1016/j.msea.2018.09.079.
[26] G.T. Gray, C.M. Knapp, D.R. Jones, V. Livescu, S. Fensin, B.M. Morrow, C.P. Trujillo, D.T. Martinez, J.A. Valdez, Structure/property characterization of spallation in wrought and additively manufactured tantalum, AIP Conference Proceedings **1979**, 060002, 2018. https://doi.org/10.1063/1.5044799.
[27] G. Asala, J. Andersson, O.A. Ojo, Analysis and constitutive modelling of high strain rate deformation behaviour of wire–arc additive-manufactured ATI 718Plus superalloy, International Journal of Advanced Manufacturing Technology **103**, 1419–1431, 2019. https://doi.org/10.1007/s00170-019-03616-2.
[28] M. Laurençon, T. de Rességuier, D. Loison, J. Baillargeat, J.N.D. Ngnekou, Y. Nadot, Effects of additive manufacturing on the dynamic response of AlSi10Mg to laser shock loading, Materials Science and Engineering: A **748**, 407–417, 2019. https://doi.org/10.1016/j.msea.2019.02.001.
[29] G. Ganzenmüller, Dynamic behaviour of additively manufactured structures & materials : DYMAT 2022, 26th Technical Meeting Conference Proceedings, 2022. https://freidok.uni-freiburg.de/data/228460.
[30] E. Barraud, T. de Rességuier, S. Hémery, J. Cormier, Dynamic Behavior of a shock-loaded Ni-based superalloy manufactured by Laser Metal Deposition, in: Albert-Ludwigs-Universität Freiburg, Freiburg DE, pp. 43–48, 2022. https://doi.org/10.6094/UNIFR/228460.
[31] A. Laurence, J. Cormier, P. Villechaise, T. Billot, J.-M. Franchet, F. Pettinari-Sturmel, M. Hantcherli, F. Mompiou, A. Wessman, Impact of the Solution Cooling Rate and of Thermal Aging on the Creep Properties of the New Cast & Wrought René 65 Ni-Based Superalloy, in: E. Ott, A. Banik, J. Andersson, I. Dempster, T. Gabb, J. Groh, K. Heck, R. Helmink, X. Liu, A. Wusatowska-Sarnek (Eds.), 8th International Symposium on Superalloy 718 and Derivatives, John Wiley & Sons, Inc., Hoboken, NJ, USA, pp. 333–348, 2014. https://doi.org/10.1002/9781119016854.ch27.
[32] S. Gourdin, J. Cormier, G. Henaff, Y. Nadot, F. Hamon, S. Pierret, Assessment of specific contribution of residual stress generated near surface anomalies in the high temperature fatigue life of a René 65 superalloy: Effect of Surface Anomalies on the Fatigue Life of a René 65 Superalloy, Fatigue and Fracture of Engineering Materials and Structures **40**, 69–80, 2017. https://doi.org/10.1111/ffe.12475.
[33] D. Tiparti, A. Wessman, J. Cormier, S. Tin, Comparison of the stress relaxation and creep behavior of conventionally forged and additively manufactured René 65, Journal of Materials Science **58**, 5951-5969, 2023. https://doi.org/10.1007/s10853-023-08399-2
[34] M. Huguet, G. Boissonnet, G. Lotte, J. Cormier, P. Villechaise, G. Bonnet, F. Pedraza, High temperature oxidation of additively manufactured Rene 65, Corrosion Science **220**, 111273, 2023. https://doi.org/10.1016/j.corsci.2023.111273

[35] E. Lescoute, T. De Rességuier, J.-M. Chevalier, D. Loison, J.-P. Cuq-Lelandais, M. Boustie, J. Breil, P.-H. Maire, G. Schurtz, Ejection of spalled layers from laser shock-loaded metals, Journal of Applied Physics **108**, 093510, 2010. https://doi.org/10.1063/1.3500317.
[36] T. de Rességuier, E. Lescoute, A. Sollier, G. Prudhomme, P. Mercier, Microjetting from grooved surfaces in metallic samples subjected to laser driven shocks, Journal of Applied Physics **115**, 043525, 2014. https://doi.org/10.1063/1.4863719.
[37] L.M. Barker, R.E. Hollenbach, Laser interferometer for measuring high velocities of any reflecting surface, Journal of Applied Physics **43**, 4669–4675, 1972. https://doi.org/10.1063/1.1660986.
[38] A. Benuzzi-Mounaix, M. Koenig, G. Huser, B. Faral, D. Batani, E. Henry, M. Tomasini, B. Marchet, T.A. Hall, M. Boustie, T. de Rességuier, M. Hallouin, F. Guyot, D. Andrault, T. Charpin, Absolute equation of state measurements of iron using laser driven shocks, Physics of Plasmas **9**, 2466–2469, 2002. https://doi.org/10.1063/1.1478557.
[39] G. Huser, M. Koenig, A. Benuzzi-Mounaix, E. Henry, T. Vinci, B. Faral, M. Tomasini, B. Telaro, D. Batani, Temperature and melting of laser-shocked iron releasing into an LiF window, Physics of Plasmas **12**, 060701, 2005. https://doi.org/10.1063/1.1896375.
[40] D.E. Grady, The spall strength of condensed matter, Journal of the Mechanics and Physics of Solids **36**, 353–384, 1988. https://doi.org/10.1016/0022-5096(88)90015-4.
[41] T. Antoun, L. Seaman, D.R. Curran, G.I. Kanel, S.V. Razorenov, A.V. Utkin, Spall fracture, Springer, New York, 2003. https://doi.org/10.1007/b97226.
[42] E.O. Hall, The Deformation and Ageing of Mild Steel: III Discussion of Results, Proceedings of the Physycal Society B **64**, 747–753, 1951. https://doi.org/10.1088/0370-1301/64/9/303.
[43] R.W. Armstrong, Engineering science aspects of the Hall–Petch relation, Acta Mechanica **225**, 1013–1028, 2014. https://doi.org/10.1007/s00707-013-1048-2.
[44] A. Yu, X. Li, C. Jia, Z. Jiang, Influence of Grain Size on Tensile and Stress Rupture Behavior of an Advanced Wrought Ni-Based Superalloy, in: M. Chen, M. Giorgetti, Z. Li, Z. Chen, B. Jin, R.K. Agarwal (Eds.), Advances in Transdisciplinary Engineering, IOS Press, 2022. https://doi.org/10.3233/ATDE220418.
[45] F. Wei, B. Cheng, L.T. Chew, J.J. Lee, K.H. Cheong, J. Wu, Q. Zhu, C.C. Tan, Grain distribution characteristics and effect of diverse size distribution on the Hall–Petch relationship for additively manufactured metal alloys, Journal of Materials Research and Technology **20**, 4130–4136, 2022. https://doi.org/10.1016/j.jmrt.2022.09.006.
[46] E. Balikci, R.A. Mirshams, A. Raman, Tensile Strengthening in the Nickel-Base Superalloy IN738LC, Journal of Materials Engineering and Performance **9**, 324–329, 2000. https://doi.org/10.1361/105994900770345999.
[47] B. Du, L. Sheng, Z. Hu, C. Cui, J. Yang, X. Sun, Investigation on the microstructure and tensile behavior of a Ni-based IN792 superalloy, Advances in Mechanical Engineering **10**, 168781401775216, 2018. https://doi.org/10.1177/1687814017752167.
[48] E.I. Galindo-Nava, L.D. Connor, C.M.F. Rae, On the prediction of the yield stress of unimodal and multimodal γ ′ Nickel-base superalloys, Acta Materialia **98**, 377–390, 2015. https://doi.org/10.1016/j.actamat.2015.07.048.
[49] A. Sengupta, S.K. Putatunda, L. Bartosiewicz, J. Hangas, P.J. Nailos, M. Peputapeck, F.E. Alberts, Tensile behavior of a new single crystal nickel-based superalloy (CMSX-4) at room and elevated temperatures, Journal of Materials Engineering and Performance **3**, 664–672, 1994. https://doi.org/10.1007/BF02645265.

[50] R.I. Zainullin, A.A. Ganeev, R.V. Shakhov, S.K. Mukhtarov, V.M. Imayev, R.M. Imayev, Microstructure and mechanical properties of a nickel-base superalloy heavily alloyed with substitution elements, IOP Conference Series: Materials Science and Engineering **1008**, 012008, 2020. https://doi.org/10.1088/1757-899X/1008/1/012008.
[51] K. Hou, M. Wang, P. Zhao, M. Ou, H. Li, Y. Ma, K. Liu, Temperature-dependent yield strength and deformation mechanism of a casting Ni-based superalloy containing low volume-fraction γ′ phase, Journal of Alloys and Compounds **905**, 164187, 2022. https://doi.org/10.1016/j.jallcom.2022.164187.
[52] G.I. Kanel, Spall fracture: methodological aspects, mechanisms and governing factors, International Journal of Fracture **163**, 173–191, 2010. https://doi.org/10.1007/s10704-009-9438-0.
[53] B.J. Bond, R.L. Kennedy, Evaluation of Allvac 718Plus Alloy in the Cold Worked and Heat Treated Condition, in: Superalloys 718, 625, 706 and Derivatives 2005, Ed. E.A. Loria, TMS, pp. 203–211, 2005. https://doi.org/10.7449/2005/Superalloys_2005_203_211.

Declaration of interests

☒ The authors declare that they have no known competing financial interests or personal relationships that could have appeared to influence the work reported in this paper.

☐ The authors declare the following financial interests/personal relationships which may be considered as potential competing interests: